C. R. Mecanique 347 (2019) 1–18

Contents lists available at ScienceDirect

Comptes Rendus Mecanique

www.sciencedirect.com

Fully coupled hydromechanical model for compacted soils

Hiram Arroyo [a,b,*,1], Eduardo Rojas [a]

[a] Faculty of Engineering, Universidad Autónoma de Querétaro, Centro Universitario, Cerro de las Campanas, 76160 Querétaro, Qro., Mexico
[b] Department of Agroindustrial Engineering, Universidad de Guanajuato, Campus Celaya-Salvatierra, Av. Ing. Javier Barros Sierra 201, 38140 Celaya, Gto., Mexico

ARTICLE INFO

Article history:
Received 7 July 2017
Accepted 25 September 2018
Available online 6 November 2018

Keywords:
Constitutive model
Effective stress
Pore-size distribution
Retention curve
Elastoplastic deformation
Hydro-mechanical coupling

ABSTRACT

To accomplish a proper conception and further modeling of the mechanical behavior of soils, observations at the micro and macro scales need to be merged. The authors believe that the link between scales can be achieved using the effective stress concept. In this paper, we present a model that quantifies the air and water volumes contained within the pores of a solid when their pore pressure is varied. The macroscopic consequences of this are expressed in terms of a single stress that is used to formulate a simple elastoplastic constitutive model to predict volume strains and shear strength of soils.

1. Introduction

Conventional materials such as steel or concrete can be considered homogeneous from the point of view of their internal particle arrangement. Unlike soils, the tight arrangement of their individual components makes them barely compressible when they are compared to other materials such as soils. Because soils are compressible materials, the fluids in their voids largely influence their behavior and therefore, hydraulic and mechanical coupling occurs.

The aim of this paper is to propose a fully coupled effective stress constitutive model for soils that accounts for their shearing resistance as well as for the volumetric and hydraulic behavior. The main objective of this development is to show that simple fully coupled models can be built for unsaturated soils.

The authors believe by that an important element to correctly model the hydromechanical coupling of unsaturated soils lays in the correct modeling of the evolution of the pore size distribution, which in turn affects the soil–water retention curves.

The choice of a suitable stress–strain framework to describe the behavior of soils is of paramount importance. Recent developments related to constitutive modeling of soils have led researchers to conclude that there is no preferred stress framework because they all offer different features [1,2]. There are two main trends when choosing the suitable framework that may be used to derive the constitutive equations for unsaturated soils. One of them considers that the state of stress of a soil is a combination between the external stresses σ_{ij}^{t} and matric suction s. The other one, is based on the ideas established by Terzaghi [3] and Fillunger [4]. It assumes that a single stress, called the effective stress, controls their mechanical and hydraulic behavior. While Terzaghi and Fillunger settled the basis for the behavior of porous materials with

* Corresponding author.
E-mail address: hiramarroyo@hotmail.com (H. Arroyo).
[1] Current address: Universidad de Guanajuato, Campus Celaya-Salvatierra, Ing. Javier Barros Sierra 201, 38140 Celaya, Gto., México.

https://doi.org/10.1016/j.crme.2018.09.005
1631-0721/

their voids saturated with a single fluid, Bishop [5] proposes an expression for the effective stress of porous materials with two immiscible phases:

$$\sigma'_{ij} = \sigma^{t}_{ij} - u_a \delta_{ij} \chi (u_a - u_w) \delta_{ij} \tag{1}$$

In Eq. (1), σ'_{ij} represents the effective stress tensor. u_a and u_w refer to the internal air and water pressures, δ_{ij} is the Kronecker delta. The difference between air pressure u_a and water pressure u_w is known as matrix suction ($s = u_a - u_w$), whereas the term $\chi(u_a - u_w)$ is called suction stress. The sign convention for soil mechanics is adopted here: positive stresses and strains denote compressive stresses and volume reductions, respectively.

If the condition $u_a = 0$ is imposed in Eq. (1), the pore water pressure will be computed as in Eq. (2):

$$u_w = \left(\sigma^{t} - \sigma'\right)/\chi \tag{2}$$

If we assume positive values for u_w, then $\sigma^{t} > \sigma'$. This is the case for soils under saturated conditions where pore-water pressures are positive inducing outward compressive stresses on the walls of the voids contained within the soil. If we assume negative values for u_w, then $\sigma^{t} < \sigma'$. This negative stress acts as a tensile stress that tends to close the internal walls of a pore. This stress is termed matric suction and only occurs upon the appearance of air–water interfaces, that is, when the soil is in unsaturated conditions.

Here, Eq. (1) should be valid for both cases, saturated and unsaturated. To allow a smooth transition between the saturated and unsaturated states, the scalar χ must take the limiting values 0 and 1. This discussion points out the intuitive idea that χ equals the degree of saturation of the soil S_r. If this simplification is assumed, as S_r approaches zero, u_w increases indefinitely to negative values if $u_a = 0$. This is an unreal situation since this leads to cavitation of the liquid phase. Experimentally χ would be capable of being measured just before water cavitation. This is a reason to discard the condition $\chi = S_r$, since low degrees of saturation would bring conceptual and physical inconsistencies and $\chi = S_r$ would not hold. Nonetheless, it has been recognized that χ is strongly related to S_r implicitly assigning a hysteretic nature to the effective stress.

2. Hydromechanical coupling

Coupling hydraulic and mechanical behaviors for unsaturated soils is one of the most challenging tasks. This is because, as Laloui and Nuth [6] state, three levels of agreement should be accomplished. First, a suitable stress is required, which allows handling a discontinuous media such as an unsaturated soil on the ground of a continuous one. In this work, we assume the existence of an effective stress that complies with Terzaghi's classical definition. Such effective stress can be expressed as a dependency law written as a function of the stresses that arise in compacted soils, including a suction stress $u_a - u_w$ and a mean net stress $\overline{p}$. This dependency law takes the form of Eq. (1).

In terms of effective stresses, the isotropic part of the stress tensor (Eq. (1)) for the triaxial case is expressed as:

$$p' = \overline{p} + \chi s \tag{3}$$

The final ingredients to be presented are a consistent stress–strain framework and a constitutive context. In this section, we present both of them.

The model proposed herein is formulated under elastoplastic theory. The hardening equation proposed by Juárez-Badillo [7] and later modified by Rojas and Chavez [8] writes:

$$\mathrm{d}p'_0 = \frac{1 + e_0}{e} \frac{p'}{\lambda - \kappa} \mathrm{d}\varepsilon^{p}_{v} \tag{4}$$

Eq. (4) is a function of the initial void ratio e_0 and the compressibility indexes λ and κ for virgin loading and unloading–reloading, respectively. $\mathrm{d}\varepsilon^{p}_{v}$ represents the plastic volumetric strain increment. Eq. (4) resembles that used by Alonso et al. [9], with the difference that it is a function of the current void ratio of the material.

2.1. Suction hardening

The goal of this section is to describe hardening laws on the plane of effective mean stress against suction. Assume that the porous material is initially saturated and subsequently subjected to drying at constant net stress. Consider also that suction reaches the air entry value ($s = a_{ev}$). In these conditions the effective stress moves from point A to B such that $p' = p'_B$ (see Fig. 1).

Now, if the stress increment $\chi_{aev} a_{ev}$ is released (wetting), an elastic recovery occurs, although, plastic strains will endure. These plastic volumetric strains are directly related to the increment in the preconsolidation stress. When suction surpasses its maximum historical value, the plastic volumetric strains can be computed considering Eq. (4) written in the form:

$$\left(\mathrm{d}\varepsilon^{p}_{vp'}\right)_{AB} = \left(\mathrm{d}p'_0\right)_{AB} \frac{e_B}{(1 + e_A)} \frac{(\lambda - \kappa)}{p'_B} = \chi_{aev} a_{ev} \frac{e_B}{(1 + e_A)} \frac{(\lambda - \kappa)}{p'_B} \tag{5}$$

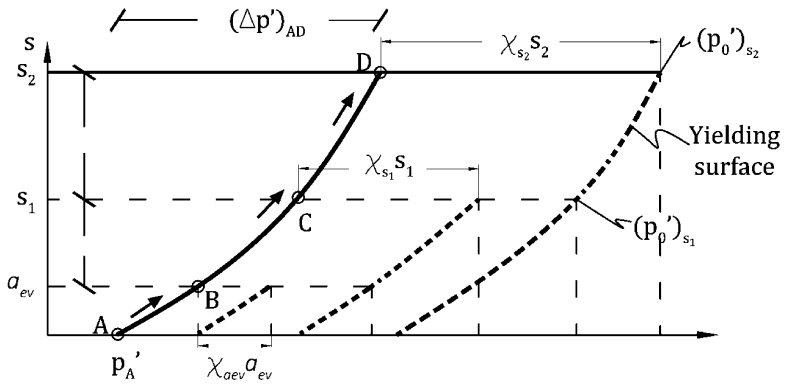

Fig. 1. Evolution of the yield surface at drying.

Eq. (5) gives information not only about the evolution of plastic volumetric strains, but also regarding the material hardening in terms of effective stress when suction is increased. Therefore, an increment in the apparent preconsolidation stress $(\mathrm{d}p'_0)_{\mathrm{AB}}$ occurs when the material shows a plastic volumetric strain $(\mathrm{d}\varepsilon^{\mathrm{p}}_{\mathrm{vp}'})_{\mathrm{AB}}$:

$$\left(\mathrm{d}p'_0\right)_{\mathrm{AB}} = \left(\mathrm{d}\varepsilon^{\mathrm{p}}_{\mathrm{vp}'}\right)_{\mathrm{AB}} \frac{(1+e_{\mathrm{A}})}{e_{\mathrm{B}}} \frac{p'_{\mathrm{B}}}{(\lambda-\kappa)} = \chi_{\mathrm{aev}} a_{\mathrm{ev}} \tag{6}$$

Fig. 1 shows the evolution of the preconsolidation stress as suction progresses.

If suction is increased up to point D, the apparent preconsolidation stress at suction s_2 will be $(p'_0)_{s_2} = p'_{\mathrm{A}} + (\Delta p')_{\mathrm{AD}} + \chi_{s_2} s_2$. As indicated in Eq. (6), $(\Delta p')_{\mathrm{AD}} = \chi_{s_2} s_2$. Therefore, the apparent preconsolidation stress at point D is $(p'_0)_{s_2} = p'_{\mathrm{A}} + 2\chi_{s_2} s_2$. Hence, the yield surface will gradually displace to the right-hand side as suction increases. This displacement is due to the phenomenon of suction hardening.

2.2. Hardening law for effective stress increments on constant suction

Assume that the yield criterion has been met in a soil sample subjected to mean net stress and suction increments, then, the plastic volumetric strain can be expressed as follows:

$$\mathrm{d}\varepsilon^{\mathrm{p}}_{\mathrm{vp}'} = \left(\mathrm{d}p'_0\right) \frac{(\lambda-\kappa)}{(1+e_0)} \frac{e}{p'} = (\mathrm{d}\overline{p} + s\mathrm{d}\chi + \chi\,\mathrm{d}s) \frac{(\lambda-\kappa)}{(1+e_0)} \frac{e}{p'} \tag{7}$$

When a sample is loaded at constant suction, the net stress increment produces a volumetric strain generated by the reduction of the sizes of the larger pores in the sample. This reduction in the size of pores, displaces the retention curves, which in turn affects the values of parameter χ. Therefore, in order to solve Eq. (7), all loads are treated incrementally and the value of $\mathrm{d}\chi$ in Eq. (7) corresponds to the value of the previous increment. With these considerations in mind, when loading occurs at constant suction, Eq. (7) reduces to:

$$\mathrm{d}\varepsilon^{\mathrm{p}}_{\mathrm{vp}'} = \left(\mathrm{d}p'_0\right) \frac{(\lambda-\kappa)}{(1+e_0)} \frac{e}{p'} = (\mathrm{d}\overline{p} + s\mathrm{d}\chi) \frac{(\lambda-\kappa)}{(1+e_0)} \frac{e}{p'} \tag{8}$$

To identify the evolution of the yielding surface at constant suction, consider a saturated soil subjected to the initial stress p'_{A}, then dried up to suction s_2 reaching point p'_{B} (see Fig. 2). At this stage, the loading collapse yield surface (LCYS) appears in the position CFD indicated in Fig. 2. If the soil is loaded with $\mathrm{d}p' = \mathrm{d}\overline{p} = \mathrm{d}(s_2\chi_{s_2})$, the stress state reaches point C on the yield surface and the soil behaves elastically.

With a further net stress increment $(\mathrm{d}p'_0)_{\mathrm{CE}} = p'_{\mathrm{E}} - p'_{\mathrm{C}} = (\mathrm{d}\overline{p} = s\mathrm{d}\chi)_{\mathrm{CE}}$, the material yields and the LCYS tilts. By computing the increment in the plastic volumetric strain, it is possible to derive the equation for the tilted yield surface. This increment is:

$$\left(\mathrm{d}\varepsilon^{\mathrm{p}}_{\mathrm{v}}\right)_{\mathrm{CE}} = (\lambda-\kappa) \frac{e_{\mathrm{E}}}{(1+e_{\mathrm{C}})} \frac{(\mathrm{d}\overline{p} - s\mathrm{d}\chi)_{\mathrm{CE}}}{(p'_{\mathrm{E}})_{s_2}} \tag{9}$$

Now, assume that a neutral loading is followed from point E to G where $e_{\mathrm{E}} = e_{\mathrm{G}}$, and from C to F where $e_{\mathrm{C}} = e_{\mathrm{F}}$. Furthermore, the increment in the preconsolidation stress for suction stress level s_3 is $(\mathrm{d}p'_0)_{s_3} = \frac{1+e_{\mathrm{F}}}{e_{\mathrm{G}}} \frac{p'_{\mathrm{G}}}{(\lambda-\kappa)} (\mathrm{d}\varepsilon^{\mathrm{p}}_{\nu})_{\mathrm{FG}}$. With these equations in addition to Eq. (9), and considering that $p'_{\mathrm{G}} = p'_{\mathrm{F}}(dp'_0)$, it can be written:

$$\left(\mathrm{d}p'_0\right)_{s_3} = \frac{1+e_{\mathrm{F}}}{e_{\mathrm{G}}} \frac{p'_{\mathrm{G}}}{(\lambda-\kappa)} \left(d\varepsilon^{\mathrm{p}}_{\nu}\right)_{\mathrm{FG}} = \frac{1+e_{\mathrm{F}}}{e_{\mathrm{G}}} \frac{p'_{\mathrm{G}}}{(\lambda-\kappa)} (\lambda-\kappa) \frac{e_{\mathrm{E}}}{1+e_{\mathrm{C}}} \frac{(\mathrm{d}\overline{p} + s\mathrm{d}\chi)_{\mathrm{CE}}}{(p'_{\mathrm{E}})_{s_2}} = \frac{p'_{\mathrm{F}}}{(p'_{\mathrm{C}})_{s_2}} (\mathrm{d}\overline{p} + s\mathrm{d}\chi)_{\mathrm{CE}} \tag{10}$$

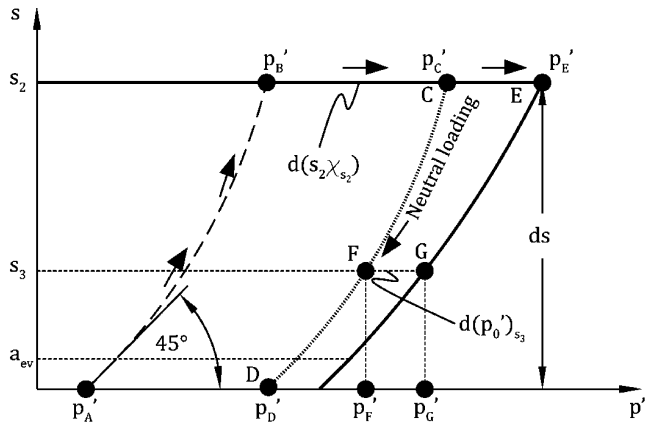

Fig. 2. Evolution of the yield surface due to the mean net stress increase.

where $(p'_C)_{s_2}$ is the stress state before yielding. In conclusion, the increment of the preconsolidation stress for suctions lower or equal to s_2 due to a net mean stress increment at constant suction is:

$$\left(\mathrm{d}p'_0\right)_{s_3} = \frac{p'_F}{(p'_C)_{s_2}}(\mathrm{d}\overline{p} + s\mathrm{d}\chi)_{CE} \tag{11}$$

Note that the amount of increment will depend on the ratio $p'_F/(p'_C)_{s_2}$. If full saturation of the sample occurs after the tilting of the LCYS, it may occur that the wetting path crosses the LCYS. This case has been extensively treated by Rojas [8,10] and shows that this elastoplastic framework is suitable for simulating the collapse upon wetting phenomenon.

With these ingredients in hand, constitutive relationships for unsaturated soils based on an elastoplastic framework can be proposed. A simple and practical model can be built, which requires a reduced number of parameters.

3. The hydraulic model

It has been shown elsewhere [8,10] that the scalar χ depends on the distribution of water and air contained in the soil mass as it undergoes wetting–drying cycles. This, of course, presents a practical difficulty, since the porous structure needs to be known with precision. These difficulties can be overcome using a porous-solid model, as described below.

Because the internal structure of soils is too complicated to be modeled, various authors joined together to simplify the geometries of pores. It has been shown [11–15] that pores can be modeled considering two main types of entities: sites and bonds, both of them contributing to the total volume of the pores. Sites contribute with most of the volume of voids and are responsible for most of the volume change of soils [16]. These elements have large sizes and therefore control the wetting process. Bonds interconnect sites and have little contribution to the volume of voids. Because these elements show smaller sizes than sites, they control the drying process.

Despite the fact that assigning regular geometries to the pores may seem rather simplistic, experimental data have shown that the critical stages of drying or wetting in regular pores resembles that of real-shaped irregular pores [17–19]. This is why authors have modeled sites and bonds in a bi-dimensional network as circles and rectangles, respectively. For tri-dimensional modeling, spheres and cylinders are implemented, respectively.

This hydraulic model has been extensively described elsewhere [20]. It is based on the behavior of the micro-structure and macro-structure expressed in terms of the description and evolution of the pore-size distribution. A suitable choice is a normal distribution function [21,22], hence, the pore-size distribution function $V_R(\mu, \sigma)$ depends only on the mean size μ and the standard deviation σ, of each entity.

In order to make the model as real as possible, the frequency of each size appearing in the porous space needs to be established. A set of published results [23–27] indicates that the frequency of the pores shows a normal distribution. Here, a normal logarithmic density function is used:

$$f(R) = \frac{1}{\sigma R\sqrt{2\pi}} \exp\left[\frac{-(\ln R - \mu)^2}{2\sigma^2}\right] \tag{12}$$

where $f(R)$ is the frequency distribution of the pores of size R contained within the porous space. Considering a bi-dimensional network where pores show circular shapes, the volume of pores of size R is given by $V = N\pi \int_R^{R+\mathrm{d}R} f(R)R^2\mathrm{d}R$, where N represents the total number of pores contained within the pore space. Fig. 3 shows a plot for the volume of pores of different sizes $(\nu(R))$. The total volume of pores within the porous network is then: $\overline{Vs} = N\pi \int_0^{\inf} f(R)R^2\mathrm{d}R$.

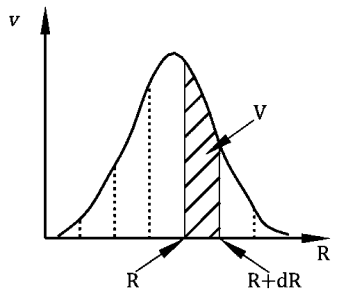

Fig. 3. Relative volume distribution evaluation.

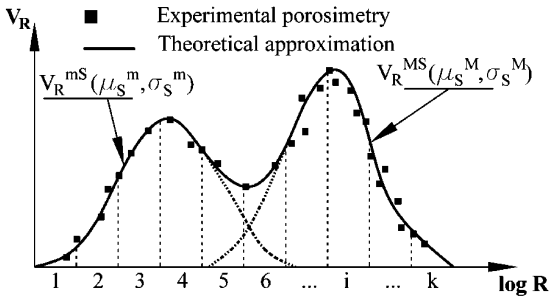

Fig. 4. Fitting the experimental pore-size distribution of a soil with the porous-solid model.

A relative volume distribution $V_{\mathrm{R}}(R)$ is defined as:

$$V_{\mathrm{R}}(R)\frac{V}{Vs}=\frac{\int_{R}^{R+\mathrm{d}R} f(R)(R^2)\mathrm{d}R}{\int_{0}^{\inf} f(R)(R^2)\mathrm{d}R} \tag{13}$$

Note that Eq. (13) is no longer a function of N. Both functions (numerator and denominator) are evaluated numerically dividing integrals in thin slices with thickness ΔR of logarithmic spacing. The convergence of the solution depends on the size of ΔR.

Compacted soils usually exhibit a bimodal pore-size distribution. To differentiate two classes of sites, the terms "macro-sites" and "micro-sites" will be used regardless other classifications. Hence, a function for macro-sites $V_{\mathrm{R}}^{\mathrm{MS}}(\mu_{\mathrm{S}}^{\mathrm{M}},\sigma_{\mathrm{S}}^{\mathrm{M}})$ and a function for micro-sites $V_{\mathrm{R}}^{\mathrm{mS}}(\mu_{\mathrm{S}}^{\mathrm{m}},\sigma_{\mathrm{S}}^{\mathrm{m}})$ are needed (see Fig. 4). The overlap between these functions depends on the soil structure. Small overlap means that the soil structure shows two very different main sizes of cavities: one for the macrostructure and another for the microstructure. Furthermore, different functions for macro-bonds $V_{\mathrm{R}}^{\mathrm{MB}}(\mu_{\mathrm{B}}^{\mathrm{M}},\sigma_{\mathrm{B}}^{\mathrm{M}})$ and micro-bonds $V_{\mathrm{R}}^{\mathrm{mB}}(\mu_{\mathrm{B}}^{\mathrm{m}},\sigma_{\mathrm{B}}^{\mathrm{m}})$ will be needed too. To complete the description of the material, solids are also required. Two functions can be used for this purpose one for large grains $V_{\mathrm{R}}^{\mathrm{SOLM}}(\mu_{\mathrm{S}}^{\mathrm{SOLM}},\sigma_{\mathrm{S}}^{\mathrm{SOLM}})$ and other for small particles $V_{\mathrm{R}}^{\mathrm{SOLm}}(\mu_{\mathrm{S}}^{\mathrm{SOLm}},\sigma_{\mathrm{S}}^{\mathrm{SOLm}})$. Functions $V_{\mathrm{R}}^{\mathrm{SOLM}}$ and $V_{\mathrm{R}}^{\mathrm{SOLm}}$ are obtained when the combined values of $\mu_{\mathrm{S}}^{\mathrm{SOLM}}$, $\sigma_{\mathrm{S}}^{\mathrm{SOLM}}$, $\mu_{\mathrm{S}}^{\mathrm{SOLm}}$ and $\sigma_{\mathrm{S}}^{\mathrm{SOLm}}$ are such that they fit the grain-size-distribution curve of the soil.

With this information, it is possible to determine the number of pores of each size needed to fill a porous grid of a certain size. A regular grid is chosen to place at random the different entities of the model (sites, bonds and solids) (Fig. 5b). The full process to create the network has been described elsewhere [20].

Once the network is set up, it is possible to simulate wetting–drying processes as suction changes. During a wetting process, all pores are initially dried, then suction is reduced by steps, and the grid is analyzed to identify those cavities that can be filled with water (see Fig. 5a). This is done by identifying those cavities that comply with the following rules that let pores saturate [22]: (a) its radius R must be smaller than the critical value R_{C} given by the Young–Laplace equation, and (b) it must be connected to the bulk of water following a continuous path from the boundaries.

The Young–Laplace equation writes $s=u_{\mathrm{a}}-u_{\mathrm{w}}=2T_s\cos\phi/R_{\mathrm{C}}$, where ϕ is the contact angle that is usually considered as 0 [13] and $T_s=7.36$ N/m represents the air–water interfacial tensional force. Hence, the critical radius can be computed as follows:

$$R_{\mathrm{C}}=\frac{2T_s\cos\phi}{s} \tag{14}$$

For the case of a drying process, a site will dry when it complies with the following conditions: (a) the radius R of the site is larger than the critical radius R_{C} and (b) it must be connected to the boundaries by a continuous path of dried pores.

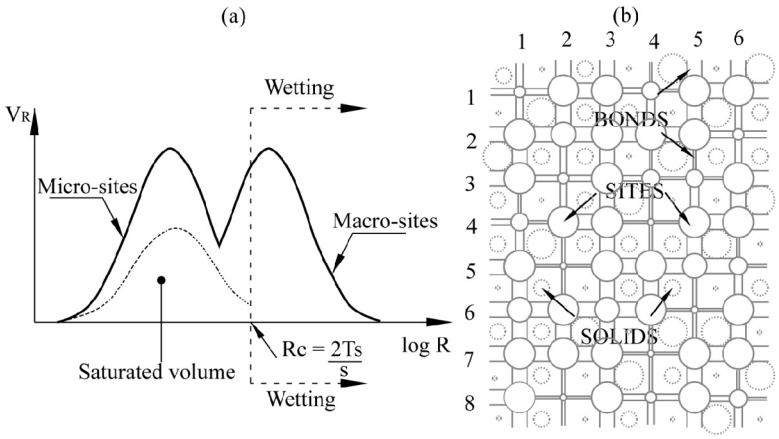

Fig. 5. (a) Wetting–drying processes simulated from a certain PSD. (b) Rectangular grid built with a characteristic frequency distribution and grain-size distribution.

With every suction increase/decrease, the rectangular grid is analyzed to search for sites that comply with these two conditions during a drying or wetting path, respectively. It can be seen from Fig. 5a that the total volume supersedes the saturated volume of pores. This is because not all sites able to saturate or dry according the Young–Laplace equation fulfill the second condition.

Solids are also considered at every suction step to compute the saturated and the dry fractions – Eq. (15) and Eq. (16), respectively. Saturated solids are defined as those grains exclusively surrounded by saturated pores. Similarly, dry solids are defined as those grains exclusively surrounded by dry pores. The total volume of the material is constituted by the volume of solids and the volume of cavities ($V = V_{SOL} + V_v$). The volume of the saturated sites V_v^s is constituted by water-filled pores that surround the saturated solids with volume V_{SOL}^s. The volume of dry sites V_v^d is constituted by dry pores surrounding dry solids V_{SOL}^d. Finally, the unsaturated fraction can be obtained from the condition that the addition of all fractions is one (Eq. (17)).

$$\varphi^s = \frac{V_{SOL}^s + V_v^s}{V} \tag{15}$$

$$\varphi^d = \frac{V_{SOL}^d + V_v^d}{V} \tag{16}$$

$$\varphi^u = 1 - \varphi^s - \varphi^d \tag{17}$$

The degree of saturation of the unsaturated fraction plays a major role in the model formulation, and it is defined as:

$$S_r^u = V_w^u / V_v^u \tag{18}$$

Here, V_w^u represents the volume of pores of the unsaturated fraction that are filled with water. V_v^u stands for the volume of cavities of the unsaturated fraction.

Notice that the volume of bonds is not taken into consideration for the computation of the fractions. This is because their contribution to the total volume of pores is negligible compared to that of the sites. It is even rather difficult to detect their volume by the mercury intrusion porosimetry tests. However, they play a major role in correctly simulating wetting/drying cycles. The fact that a unique pore-size distribution can be derived from the soil–water retention curves (SWRCs) is used to determine the functions $V_R^{MB}(\mu_B^M, \sigma_B^M)$ and $V_R^{mB}(\mu_B^m, \sigma_B^m)$. This means that wetting and drying retention curves maintain a one-to-one relationship with the pore-size distribution [28,29]. Because the imbibition process is controlled by larger pores [20], the fitting of the wetting curve is made by iteratively modifying parameters μ_S^M, σ_S^M, μ_S^m, and σ_S^m until the best fit is obtained (see Fig. 6).

Similarly, the drying curve is fitted, but this time by modifying the values for parameters μ_B^M, σ_B^M, μ_B^m, and σ_B^m.

When the void ratio modifies due to stress increments, the values of parameters ϕ^s, ϕ^d, ϕ^u, and S_r^u change [30]. Therefore, the values of V_R for sites and bonds also change.

Fig. 7a shows the PSD of a bentonite/sand mixture as a function of the material density. When comparing the PSDs of samples compacted at 1.67 and 1.97 ton/m^3, the denser sample exhibits a smaller volume of a first class of pores contained between 1 and 300 microns, while those contained between a second class of pores (ranging between 0.003 and 0.1) slightly increase. In addition, the peak of the first class of pores of the denser sample displaces from 50 to 10 microns.

Fig. 7b shows the PSDs of two samples of a clayey soil subjected to two different suctions. One of the samples was initially subjected to 1000 kPa and then its suction reduced until the saturated condition was reached. Notice that the saturated sample exhibits a smaller volume of the pores contained between 4 and 20 microns. This volumetric reduction is

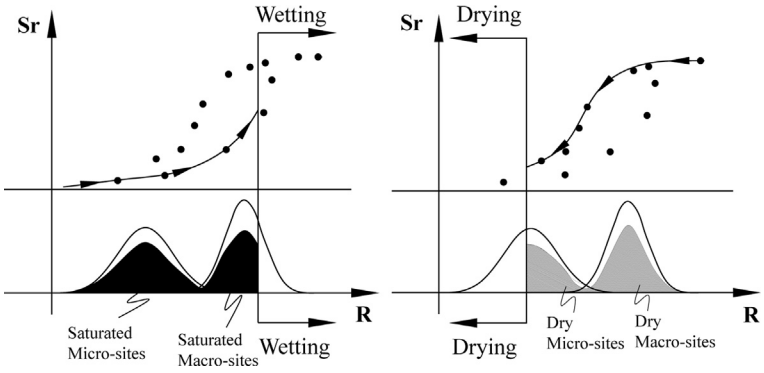

Fig. 6. Recovering the material pore-size distribution from the SWRC.

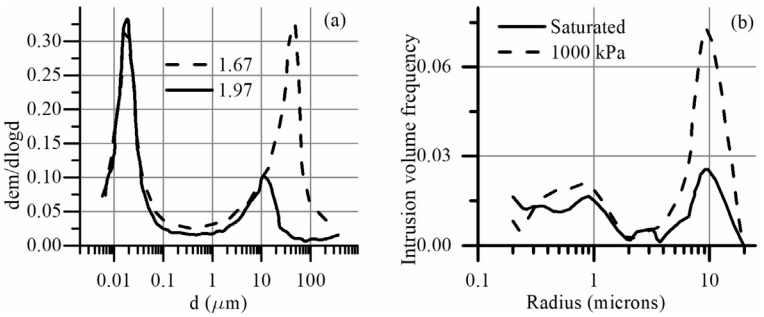

Fig. 7. (a) Pore size distribution of bentonite/sand mixtures compacted to different dry densities with a water content of about 11.0% (experimental data from Wang et al. [33]). (b) Clayey soil containing kaolin minerals (experimental data after Thom, Sivakumar, Sivakumar, Murray and Mackinnon [23]).

termed collapse upon wetting in unsaturated soil mechanics terminology and it is due to the reduction of suction stresses (χs) as water intrudes into the pores of the soil [31,32].

From these experimental reports, two observations can be made.

1. As the soil compresses due to collapse, the larger pores reduce in size and, consequently, their distribution displaces to smaller sizes and consequently reduces its peak value.
2. Because of the collapse of large pores, the distribution of the small pores apparently increases.

Many assumptions and improvements can be made to model the volume change, however, for the sake of simplicity, the volume change is related to the displacement of the $V_{\mathrm{R}}^{\mathrm{MS}}$ function. Moreover, it is assumed that only the mean size of larger sites changes ($\mu_{\mathrm{S}}^{\mathrm{M}}$). A complete description of the influence of volume change on the retention curves and its implementation is reported elsewhere [20].

3.1. Evaluation of parameter χ

In practice, the simplification $\chi = Sr$ is usually assumed, since the exact value of χ is difficult to obtain. Rojas [34] shows (as confirmed experimentally by Khalili and Zargarbashi [35]) that $\chi = Sr$ is not an accurate assumption, as pointed out by Nuth and Laloui [36] and Arroyo et al. [21], especially for the case of double structured soils. To evaluate χ, we propose to look into the microstructural behavior of the material.

When water changes are present in the mass of soil, air–water interfaces appear, increase, reduce, or disappear as the soil dries and wets, inducing localized additional stresses between soil grains. Because soils are extremely heterogeneous in terms of pore-size distribution (PSD), water may be trapped between relatively large grains or between packets of clay. Tensile stresses within each of these fractions contribute in their own particular way to strengthen the material.

Moreover, most soils show a bimodal structure meaning that they show a macrostructure and a microstructure. The macrostructure is formed by the arrangement of large grains and aggregates with large pores or macropores. Instead, the microstructure is formed by the internal structure of aggregates showing small pores or micropores. At certain value of suction, the largest macropores can be dry and some solids will be surrounded by dry pores forming a dry fraction. Instead, most aggregates remain saturated and represent the saturated fraction. In addition, some solids will be surrounded by a combination of dry and saturated pores; they form the unsaturated fraction. This is a general description of an elementary volume of an unsaturated soil. The addition of all these three fractions is one. Each fraction behaves differently under suction increase. For example, suction has no effect on the dry fraction. Instead, for the saturated fraction, an increase in

Table 1
Model parameters for the hydraulic model.

Hydraulic model parameters	Macro-solids		Micro-solids		Macro-sites		Micro-sites		Macro-bonds		Micro-bonds	
	μ_S^{SOLM}	σ_S^{SOLM}	μ_S^{SOLm}	σ_S^{SOLm}	μ_S^{M}	σ_S^{M}	μ_S^{m}	σ_S^{m}	μ_B^{M}	σ_B^{M}	μ_B^{m}	σ_B^{m}
	6	3.5	0.0001	6	10	2.5	0.0005	3	8	4	0.00001	13

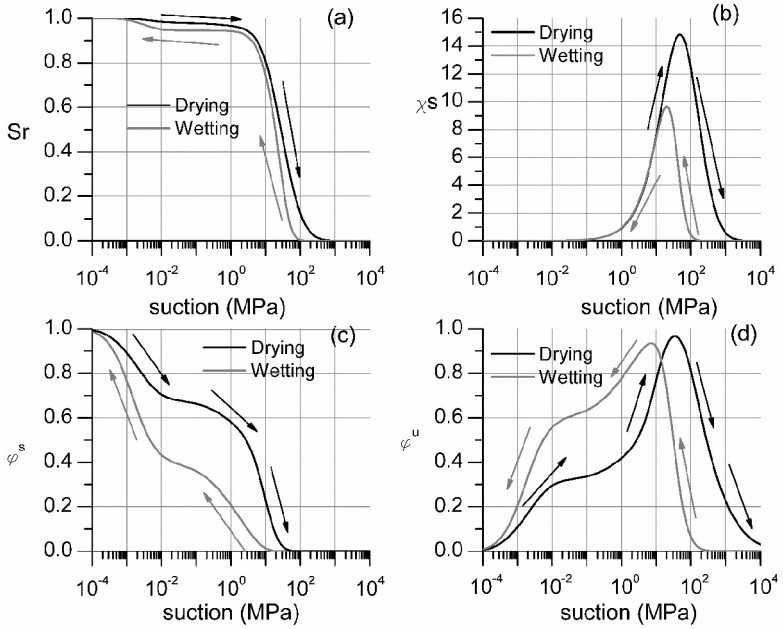

Fig. 8. Evolution of χs with saturated and unsaturated fractions during wetting drying paths. (a) Sr–s path, (b) χs during wetting and drying, (c) saturated fraction, (d) unsaturated fraction.

suction is similar to an increase in mean net stress. For this reason, it is necessary to establish the contribution of each fraction to the value of Bishop's parameter χ, indicated in Eq. (1).

Rojas [22], considered the problem of evaluating the "average" stress induced by all these constituents over an elementary representative volume of soil containing packets of clay, silt and large grains distributed in a random fashion, they all immerse in a soil mass containing air and water phases. This analysis results in Eq. (19):

$$\chi = \varphi^{s} + \varphi^{u} \cdot S_r^{u} \tag{19}$$

In Eq. (19), φ represents a soil fraction superscripts "d", "s", and "u" denote dry, saturated, and unsaturated fractions, respectively. Here, $S_r^{s} = Vw^{s}/Vv^{s}$, $S_r^{u} = Vw^{u}/Vv^{u}$ and $S_r^{d} = Vw^{d}/Vv^{d} = 0$ are the relation between the volume of water and the volume of voids that form the corresponding fraction.

The parameters involved in Eq. (19) are retrieved from a hydraulic model as presented in section 3.

Hydromechanical coupling is achieved through evaluating parameter χ. Fig. 8a shows the SWRC of a soil with the parameters reported in Table 1. Fig. 8b shows the evolution of χs in wetting–drying trajectories. Fig. 8c and d allow the reader to visualize the influence of the porous parameters, of which χ is a function.

From Fig. 8b and d, it can be seen that there is a clear relationship between the peaks of the suction stress (χs) and the unsaturated fraction (φ^{u}). Observe that the range of suction for the SWRC goes from 0.001 MPa to 400 kPa. It can be observed that the maximum suction stress appears at a lower value of suction for the wetting path than for the drying path. In addition, the suction stress is larger during drying than during wetting. This happens because the drying path occurs at larger values of suction.

It has been shown that the parameters involved in the function $\chi(\varphi^{s}, \varphi^{u}, S_r^{u})$ depend on the pore-size distribution of the material. Even if suction remains constant, χ can be stress-affected due to hydromechanical coupling. This phenomenon means that an increment of net stresses reduces the size of macropores, which in turn affects the value of χ. Consequently, and according to Eq. (20), this will induce additional volumetric strains.

Hydromechanical coupling can be easily introduced in the model as the SWRC depends on the size of pores. Hence, after computing the volumetric strains produced by an increase in the effective stress, a new pore size distribution can be established by considering that only macropores reduce in size. This reduction in the size of the macropores generates new retention curves. This implies that suction stress keeps modifying with each variation in volumetric strains and, at the same time, generates additional volumetric strains.

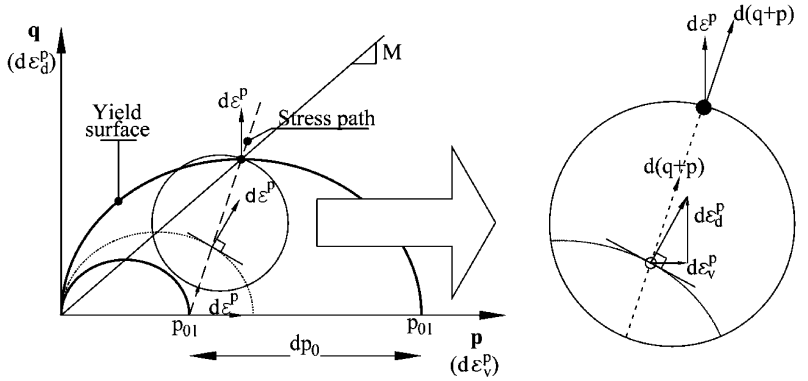

Fig. 9. Yield surfaces and hardening process in the (p, q) space.

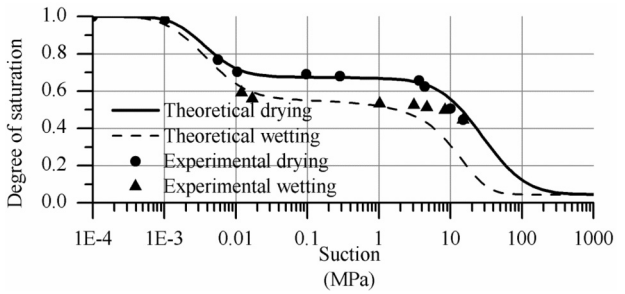

Fig. 10. Fitting to the experimental SWRC of a residual gneiss [21]. Experimental data reported by Futai and Almeida [39].

4. Stress–strain relations (mechanical model)

The model is written in terms of the usual variables, i.e. the deviator stress $q = \sigma_1 - \sigma_3$ and the mean effective stress $p' = (\sigma_1' + 2\sigma_3')/3$. As stated by Wood [37], the ingredients needed to build an elastoplastic mechanical model are the elastic properties, a yield surface, a plastic potential, and a hardening rule.

Here, the yield function in the (p, q) stress plane proposed by Roscoe and Burland [38] will be used in addition to an associated flow rule. The ellipse-shaped yield surface requires a single hardening parameter p_0.

Considering Eq. (4) and according to the modified critical state model, the stress–strain relationship for plastic stages can be expressed in matrix form as follows:

$$\begin{bmatrix} \mathrm{d}\varepsilon_{\mathrm{v}}^{\mathrm{p}} \\ \mathrm{d}\varepsilon_{\mathrm{d}}^{\mathrm{p}} \end{bmatrix} = -\frac{1}{-M^2 p'(p_0' \frac{(1+e_0)}{e(\lambda-\kappa)})} \begin{bmatrix} M^2(2p' - p_0') & 2q \\ 2q & \frac{4q^2}{M^2(2p'-p_0')} \end{bmatrix} \begin{bmatrix} \mathrm{d}p' \\ \mathrm{d}q \end{bmatrix} \tag{20}$$

In Eq. (20), $\mathrm{d}\varepsilon_{\mathrm{d}}^{\mathrm{p}}$ represents the plastic deviator strain increment, M is the slope of the critical state line (CSL). For the elastic stress–strain relationship, nonlinear behavior is disregarded at this stage and first-order elasticity is used:

$$\begin{bmatrix} \mathrm{d}\varepsilon_{\mathrm{v}}^{e} \\ \mathrm{d}\varepsilon_{\mathrm{d}}^{e} \end{bmatrix} = \begin{bmatrix} \kappa \frac{e}{(1+e_0)p'} & 0 \\ 0 & \frac{1}{3G} \end{bmatrix} \begin{bmatrix} \mathrm{d}p' \\ \mathrm{d}q \end{bmatrix} \tag{21}$$

In Eq. (21), G stands for the elastic shear modulus, $\mathrm{d}\varepsilon_{\mathrm{v}}^{e}$ and $\mathrm{d}\varepsilon_{\mathrm{d}}^{e}$ represent the increments of elastic volumetric and deviator strains, respectively. Fig. 9 sums up all the features of the proposed model in the (p, q) stress space.

5. Comparison of the numerical and experimental results

5.1. Residual gneiss

Parameters for both the hydraulic and mechanical model need to be established. For the hydraulic model, a fitting procedure is carried out to retrieve the V_{R} functions. Fig. 10 depicts with triangles and circles some experimental points of the SWRCs during wetting and drying, respectively. Undisturbed soil samples composed of residual gneiss containing 46% of clay, 9% of silt and 45% of sand were used for the experimental program. The data are provided by Futai and Almeida [39]. The parametric analysis has been described elsewhere [21]. The best fit for the retention curves was obtained with the values contained in Table 2.

Table 2
Model parameters for the hydraulic model [21].

Hydraulic model parameters	Macro-solids		Micro-solids		Macro-sites		Micro-sites		Macro-bonds		Micro-bonds	
	μ_S^{SOLM}	σ_S^{SOLM}	μ_S^{SOLm}	σ_S^{SOLm}	μ_S^{M}	σ_S^{M}	μ_S^{m}	σ_S^{m}	μ_B^{M}	σ_B^{M}	μ_B^{m}	σ_B^{m}
	6	3.5	0.0001	6	10	2.5	0.0005	3	8	4	0.00001	13

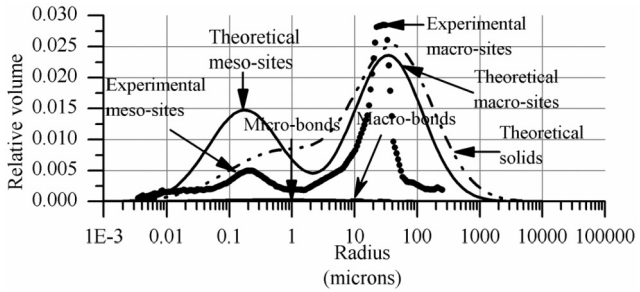

Fig. 11. Fitting to the experimental pore-size distribution of a soil [21]. Experimental data reported by Futai and Almeida [39].

Table 3
Parameters for the mechanical model [21].

Normal compression slope	Loading–reloading compression slope	Saturated preconsolidation stress (MPa)	Shear modulus (MPa)	Critical state line slope
λ	κ	$(p_0')_{sat}$	G	M
0.2	0.005	0.1	10	1.14

The best fit for the SWRC is also plotted in Fig. 10. The experimental program included a pore-size distribution performed on undisturbed samples of the same soil. The results arising from these tests are plotted in Fig. 11 along with the V_R functions obtained from the fitting process (depicted in Fig. 11 as well). The V_R functions for the solid phase are obtained by fitting the grain-size distribution curve of the material using a similar procedure as for the SWRC.

The parameters for the mechanical model are shown in Table 3. They were obtained from a series of triaxial compression tests on saturated undisturbed samples reported elsewhere [39].

The friction angle is related to the critical state slope through the relationship $M = 6\sin\phi/(3-\sin\phi)$. $(p_0')_{sat}$ is the preconsolidation stress when the suction of the material is zero.

The testing procedure for triaxial tests consisted of three stages: suction equalization, isotropic compression, and shearing stage. Samples were set in an equalization cell where an air pressure was applied from the top. A high air-entry ceramic disc located at the base of the cell allowed water to drain. This equalization stage modified the preconsolidation stress of soil samples. At the end of equalization, samples were transferred to a triaxial cell.

In general, it is difficult to determine accurately the preconsolidation stress p_0' of undisturbed samples and the initial position of the LCYS. Here, it is assumed that the soil reached its stress state departing from a saturated condition. In such a case, the stress path moves from point A to point B. Compression due to suction increase induces changes in the initial SWRC (see Fig. 12).

For the case of a sample subjected to a suction of 0.3 MPa, the effective stress state at the end of the equalization stage equals $p_A' + (\Delta p')_{A-B} = 0.1 + 0.19 = 0.29$ MPa. In addition, the preconsolidation stress due to this suction increment is (according to Fig. 1) $(p_0)_{0.3}' = p_A' + 2(\varphi^s + S_r^u\varphi^u)_{0.3}(u_a - u_w) = 0.1 + (2)0.963(0.3) = 0.478$ MPa.

Notice that the behavior of the stress path AB and that of curves LCYS0 and LCYSf is rather linear. This behavior is reserved for saturated states [1], but the sample is clearly beyond the "aev". Let us explain this. As stated by Peron et al. [40], on samples subjected to free desiccation, the larger volume strains are expected very close to full saturation. This enables us to consider that beyond $s = 0.002$ MPa, volume strains can be neglected to some extent ($\Delta V = \Delta V_v \approx 0$). Indeed, if we consider no volume change, differentiating Eq. (19) leads us to:

$$\frac{d\chi}{ds} = \frac{1}{V}\left(\frac{d(Vs^s + Vsol^s)}{ds} + \frac{d(Vs^u + Vsol^u)}{ds}Sr^u + \frac{dSr^u}{ds}\left(Vs^u + Vsol^u\right)\right) \tag{22}$$

According to Eq. (22) $d\chi$ depend on the change of Vs^s and Vs^u. Here, the only way to achieve $d\chi/ds = 0$ is by preventing changes of Vs^s and Vs^u. We can observe that between $s = 0.02$ MPa and $s = 1.0$ MPa, $\frac{dSr^u}{ds} = \frac{1}{V_V}\frac{dV_w}{ds} = \frac{1}{V_V}\frac{d(Vw^s + Vw^u)}{ds} \approx 0$, hence, Vs^s and Vs^u remain unchanged and so will $Vsol^s$ and $Vsol^u$. With this in mind, we can conclude that, if $dSr^u/ds = 0$, $d\chi/ds = 0$. Fig. 13 depicts the evolution of χ with suction, where it is confirmed that χ does not change within this suction range.

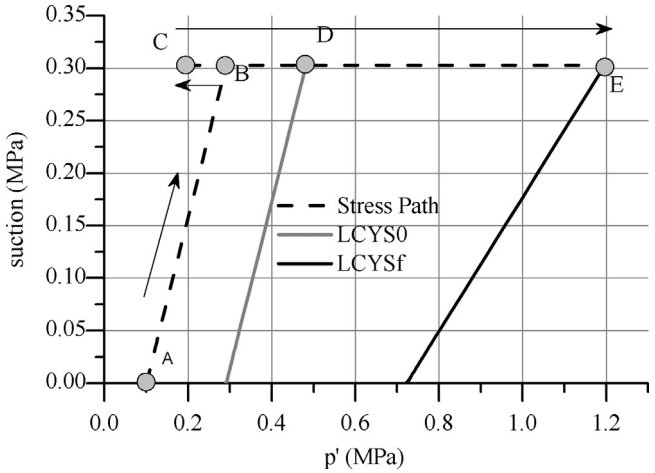

Fig. 12. Stress path followed for samples subjected to loading after drying. LYCS0 is the position of the yielding surface after suction equalization. LCYSf is the final position of the yielding surface after loading.

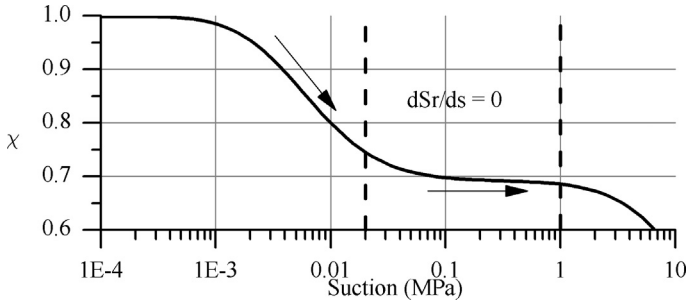

Fig. 13. Variation of χ when drying.

Therefore, the product χs will actually evolve as suction times a constant, exhibiting a straight line with slope χ that remains unchanged up to $s = 1.0$ MPa.

Now, suction has no influence on the degree of saturation within this range because the distribution of bonds is between the two large distributions of sites (see Fig. 11). Of course, if a site is surrounded by smaller bonds, this will prevent it from drying, and it will not do so until suction reaches such a value that dries at least a surrounding bond. As previously stated, the volume of bonds can be neglected. Therefore, almost no change in the degree of saturation is observed between the suction states we are interested in.

Once samples were suction-equalized (at $s = 0.3$ MPa), they were transferred to a triaxial chamber where a mean net stress of 0.005 MPa was applied (Futai and Almeida [39]). As the effective stress increment from point A to point B ($p'_B - p'_A$) $= 0.19$ MPa remains when the sample is transferred from the first chamber to the second, the initial mean effective stress in the last chamber was $p'_C = 0.005 + 0.19 = 0.195$ MPa (point C in Fig. 12). Then a mean net stresses of 0.1 MPa was applied to reach point E in Fig. 11. Plastic and elastic strains can be computed using Eqs. (20) and (21). The evolution of the yielding surface is calculated using Eq. (11). The same equalization–loading procedure was carried out for all samples tested at a suction of 0.1 MPa. Comparisons between theoretical and experimental results are plotted in Fig. 14.

A set of four triaxial tests on saturated samples was carried out. Fig. 15a depicts the stress path followed by these samples where the initial configuration of the yield surface $\bar{f}$ is shown. Fig. 15b shows the numerical (N) stress–strain relationships compared with the experimental (E) results reported by Futai and Almeida [39]. According to the results for the saturated sample shown in Fig. 11, a confining stress of 0.1 MPa generates a normally consolidated sample. The same occurs for the rest of the samples subjected to larger confining stresses.

A set of three triaxial tests was carried out for suctions $s = 0.30$ MPa and $s = 0.10$ MPa. The results of these tests are shown in Figs. 16 and 17, respectively, in terms of effective stress. For the case $s = 0.30$ MPa, the suction stress is given by the value $0.3(\varphi^s + S_r^u \varphi^u) = 0.19$ MPa. The stress–strain comparisons between the numerical and experimental results in terms of mean net stress are plotted in Figs. 16 and 17.

In order to visualize the influence of volumetric strains on the hydraulic properties of the sample subjected to $s =$ 100 kPa, Fig. 18 depicts the experimental drying SWRCs at the “initial conditions” and at the end of the shearing stage for a confining stress $\overline{p} = 200$ kPa. The black circle shows the degree of saturation of the soil sample before triaxial compression. The gray circle shows the evolution of the degree of saturation at the end of the shearing stage for the sample subjected

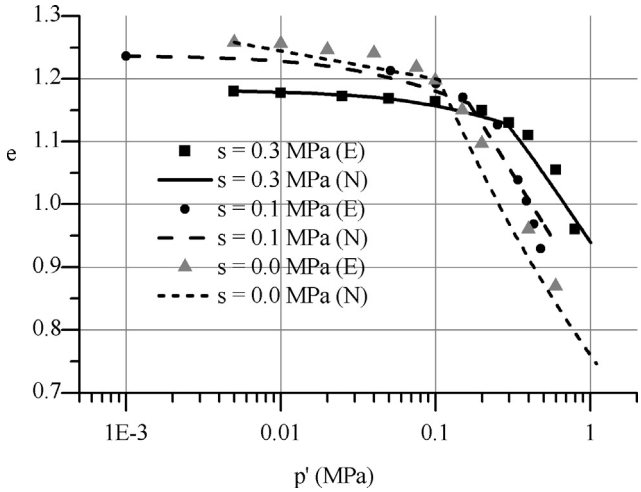

Fig. 14. Comparison of numerical (N) and experimental (E) results for samples subjected to isotropic compression. Experimental data after Futai and Almeida [39].

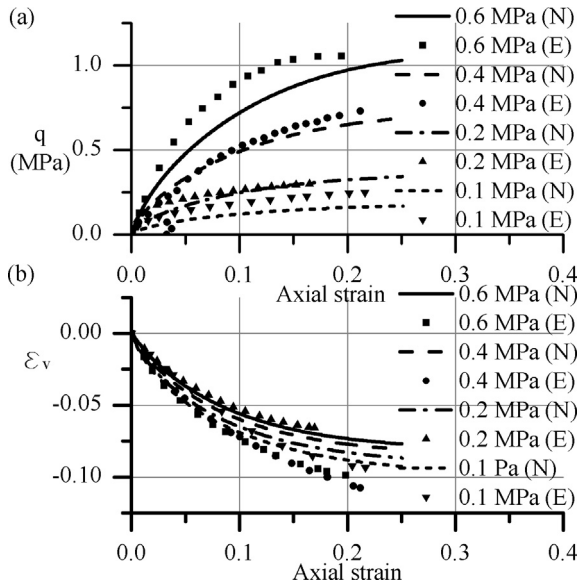

Fig. 15. Stress–strain relationship of saturated samples subjected to triaxial compression. (b) Relationships between numerical (N) and experimental (E) stress–strain results. Experimental results reported by Futai and Almeida [39].

to $\overline{p} = 200$ kPa. Notice that the model predicts full saturation at the end of the shearing stage. Unfortunately, Futai and Almeida [39] did not report the final degree of saturation of the samples.

5.2. Silty sand

Remolded samples of a soil containing 50% silt and 50% sand were tested at the School of Civil and Environmental Engineering at the University of New South Wales. The experimental program was hosted by Prof. Nasser Khalili. Samples with a void ratio of 0.8 were taken from the construction site of the Lyell dam located in the central-western part of Australia.

The preparation of the material involved a stage of oven-drying for at least 24 h. Then, the soil was prepared at a water content of 8%. Bags containing the wet soil were sealed for at least 48 h. Samples 10 cm in height and 5 cm in diameter were statically compacted at a speed rate of 0.23 mm/min.

To retrieve the V_R function for this soil, a fitting procedure was carried out with the experimental SWRCs in the same way as described earlier in this paper. Fig. 19 depicts in small triangle-shaped markers, experimental data of the SWRC. This is a drying-wetting cycle that departs from the as-compacted condition.

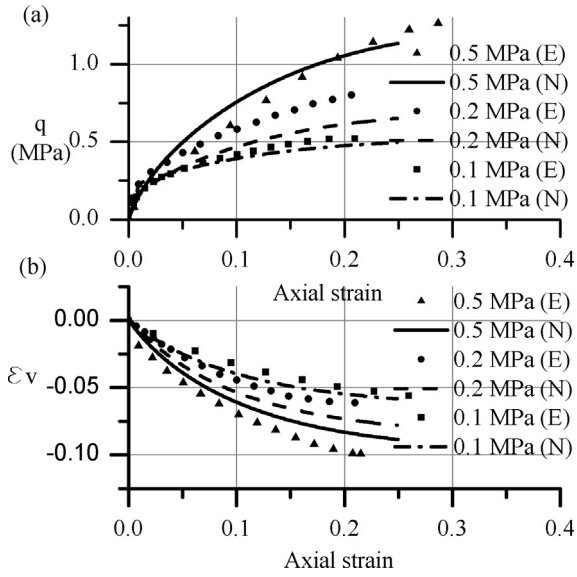

Fig. 16. (a) Stress path followed by samples subjected to $s = 0.30$ MPa in triaxial compression. (b) Deviator stress vs. axial strain, (c) Volumetric strain vs. axial strain for different mean net stresses.

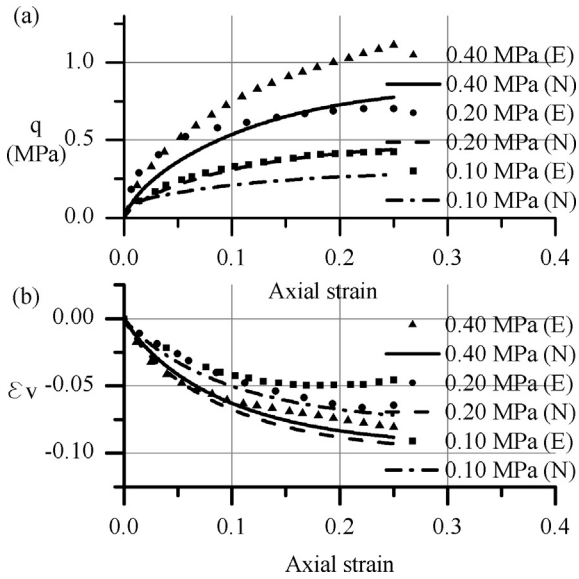

Fig. 17. (a) Stress path followed by samples subjected to $s = 0.10$ MPa during triaxial compression. (b) Deviator stress vs. axial strain (up), (c) volumetric strain vs. Axial strain for different mean net stresses.

Using the filter paper technique [41], an initial mean suction of 0.056 MPa was determined for these samples. The wetting SWRC was obtained using the axis translation technique [42]. Air at a pressure of up to 0.70 MPa was injected into a chamber provided with a pressure transducer and a high air entry ceramic disc of 15 bar at the bottom. The sample was initially subjected to a suction of 0.70 MPa from the as-compacted conditions. Then, water could drain into the sample by reducing the air pressure up to a value of 0.010 MPa to obtain the wetting path.

The grain-size distribution of the material is shown in Fig. 20. Best fits for both the wetting SWRC and the grain-size distribution were obtained using the values indicated in Table 4.

With this information it is possible to set up the porous-solid network used to simulate wetting–drying paths. The best fit for the SWRC is also plotted in Fig. 19. The main drying curve was obtained considering that the initial part corresponds to a scanning curve, as explained elsewhere [21]. This arises from experimental observations: when samples suffer compression during the preparation stage, later they show elastic recovery before they are placed in the equalization cell. In agreement with the description of the porous model, the volumetric recover increases the size of macrosites. The latter translates into a reduction of the degree of saturation $Sr = wSs/e$ of the material (where w is the water content and Ss is the solids

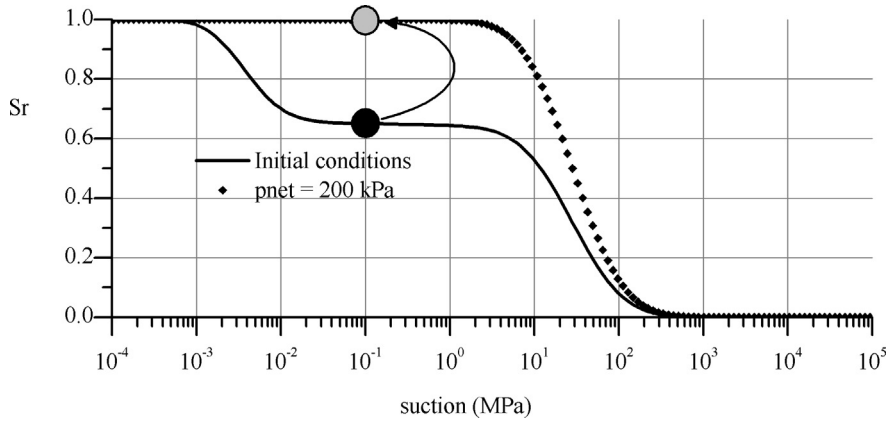

Fig. 18. Drying SWRC evolution with volume strains.

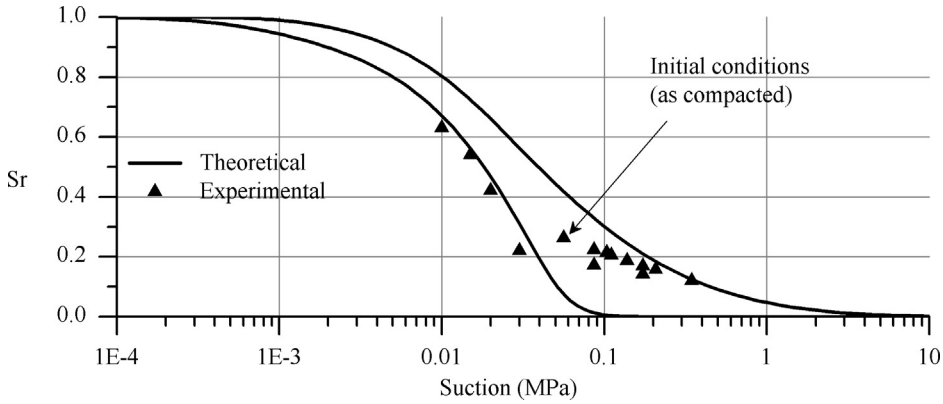

Fig. 19. A fitting to the experimental SWRC of a silty sand.

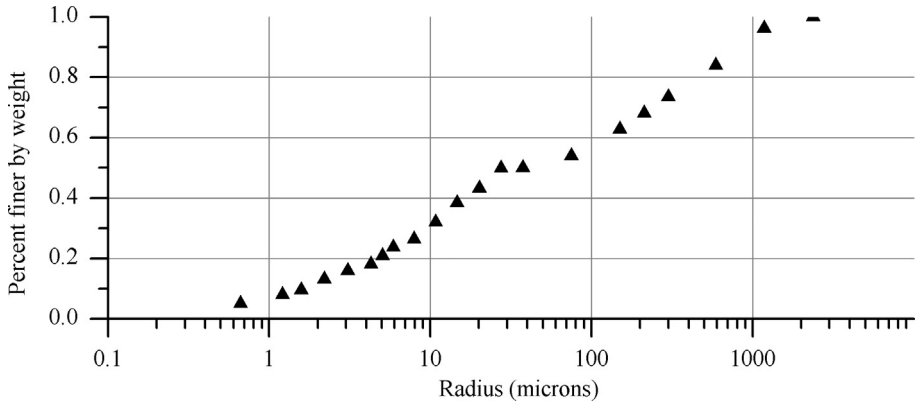

Fig. 20. Experimental grain-size distribution of the soil.

Table 4
Model parameters for the hydraulic model [21].

Hydraulic model parameters	Macro-solids		Micro-solids		Macro-sites		Micro-sites		Macro-bonds		Micro-bonds	
	μ_S^{SOLM}	σ_S^{SOLM}	μ_S^{SOLm}	σ_S^{SOLm}	μ_S^{M}	σ_S^{M}	μ_S^{m}	σ_S^{m}	μ_B^{M}	σ_B^{M}	μ_B^{m}	σ_B^{m}
	6.0	3.5	0.01	6.0	1.3	4.0	0.5	3.0	7.0	4.0	0.0001	13.0

density). This phenomenon, along with the increase in size of the pores due to volumetric recovery, tends to increase suction. With these ideas in mind, it is possible to say that the initial conditions of samples are in fact a drying scanning path that begun when the final compressive stress was released (see Fig. 19). Hence, the fitting procedure to retrieve the parameters for the main drying curve is carried out assuming that the experimental results are showing a scanning curve

Table 5
Model parameters for the mechanical model [21].

Normal compression slope	Loading–reloading compression slope	Saturated preconsolidation stress (MPa)	Shear modulus (MPa)	Critical state line slope
λ	κ	$(p'_0)_{sat}$	G	M
0.1	0.011	0.15	10	1.374

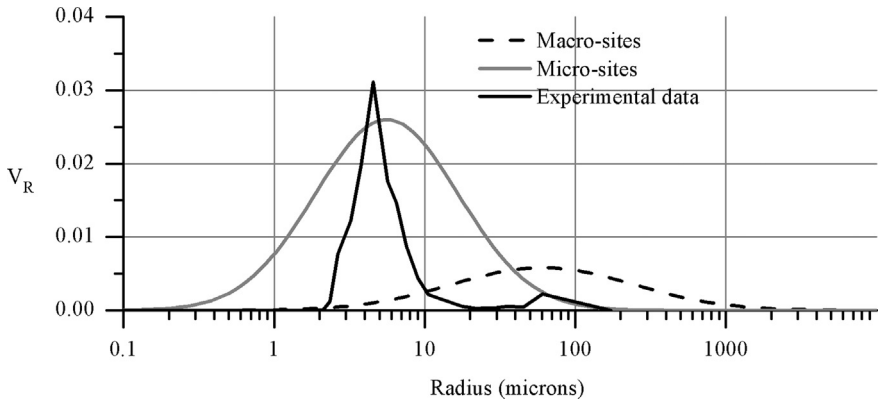

Fig. 21. Fitting to the experimental pore-size distribution of a soil.

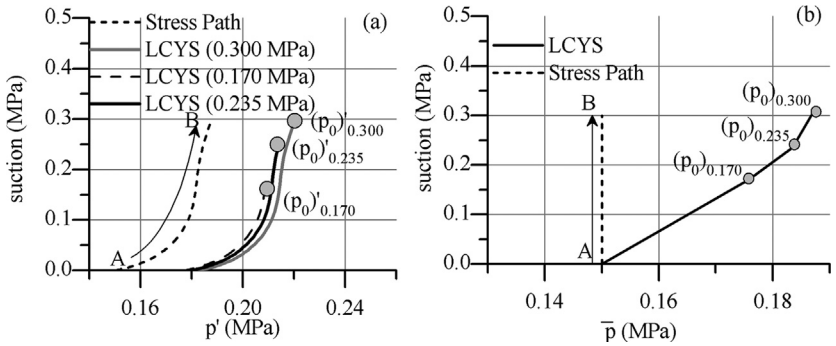

Fig. 22. Stress path followed for samples subjected to isotropic compression.

that further aligns with the main drying curve. The convenience of these assumptions will be further evaluated when the model's predictions are compared with the experimental observations. However, a more complete study, evaluation, and description of this consideration has already been made available elsewhere [21].

Again, model parameters were obtained from a series of triaxial saturated tests and are displayed in Table 5. The experimental program included pore-size distribution tests performed on samples of the same soil with an Autopore IV 9500 series. The results of these tests are plotted in Fig. 21 along with V_R functions obtained from the parametric analysis. It can be observed that the experimental and numerical main values approximately correspond; however, the numerical V_R function shows a larger range of pores sizes.

The mechanical testing procedure consisted of three stages: suction equalization (up to 0.300, 0.235, and 0.170 MPa), isotropic compression, and shearing stage. The same procedure as that applied for the simulation of the experimental results of the residual gneiss in the previous section has been used for these samples. Fig. 22b shows the stress path in terms of mean net stresses and shows the final preconsolidation stresses imposed during drying. Here, it was considered that the equalization process can be simulated as the simultaneous increase of mean net stress and suction (path AB) departing from a saturated state (point A in Fig. 22a). As explained before, it is difficult to track down the evolution of effective stresses during the compaction procedure.

Once the corresponding suction level was reached, mean net stress increments of 0.123, 0.200, and 0.350 MPa were applied. Comparisons of the theoretical results with the experimental ones for this last stage are plotted in Fig. 23.

Then samples with suctions of 0.170 and 0.235 MPa were subjected to shearing. Two sets of triaxial tests performed at suctions $s = 0.170$ MPa and $s = 0.235$ MPa and at different confining stresses were carried out. Fig. 24 and Fig. 25 exhibit the stress–strain relationship and the volumetric behavior during the shearing stage for each value of suction.

From Figs. 24 and 25, it can be noticed that the stress–strain curves are correctly predicted by the proposed model for both suction levels. However, the model underestimates and overestimates volumetric strains for low and high confining

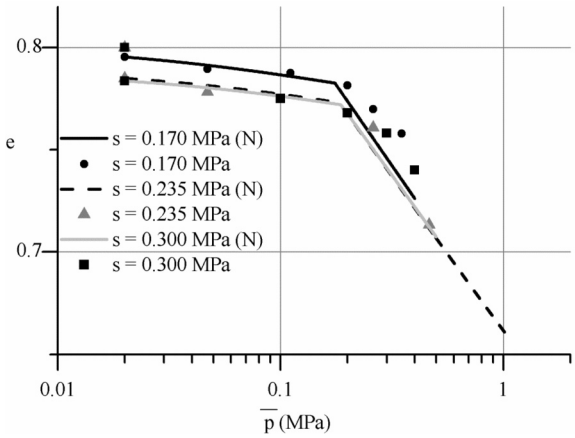

Fig. 23. Comparisons of the numerical and experimental results for samples subjected to isotropic compression.

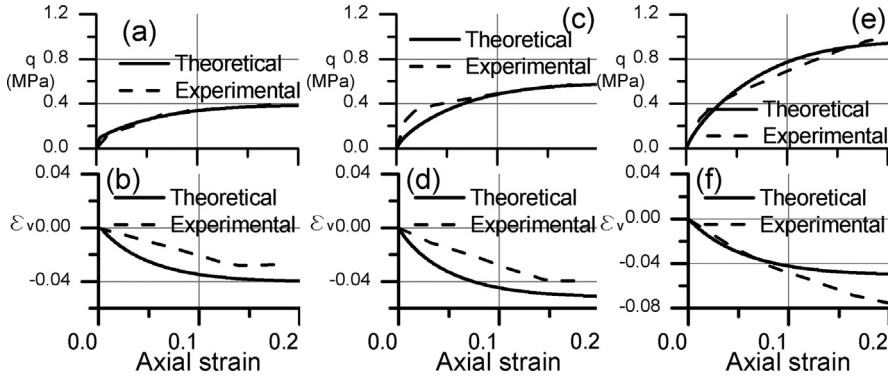

Fig. 24. Strength and volumetric behavior for samples at confined stresses of 0.123 MPa (a–b), 0.200 MPa (c–d), and 0.350 MPa (e–f).

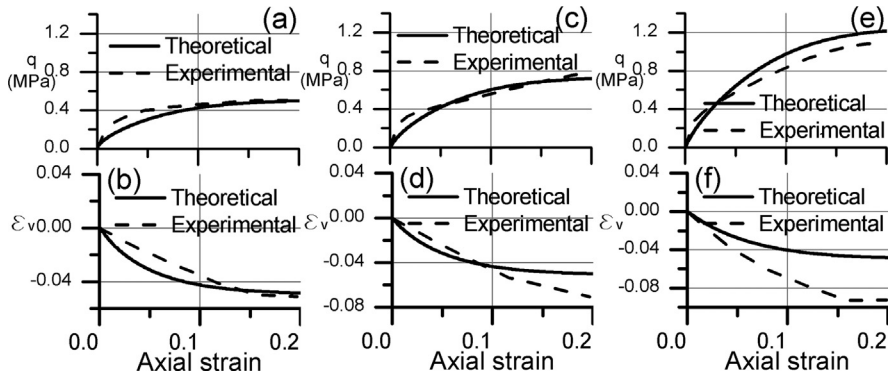

Fig. 25. Deviatoric stress vs. axial strain, volumetric strain vs. axial strain for mean net stresses of 0.167 (a–b), 0.260 (c–d), 0.465 MPa (e–f).

pressures, respectively. More sophisticated and complicated shapes for the yield surface have been shown to produce more accurate results [36,43].

Because the model used here has been maintained as simple as possible, these results show some of the limitations of the present model. In other stages of this research, different alternatives to increase the precision of the model will be explored as, for example, the shape of the yield surface [43–45], the use of non-associated flow rules [46–48], or the use of the bounding surface approach [49,50].

6. Conclusions

Because the pore-size distribution is used to predict the hydraulic behavior and the stress state of the material, the model proposed herein allows the hydromechanical coupling of compacted soils in a rather simple manner. Moreover, these ideas enlighten the comprehension of the mechanics of fabric evolution of porous materials.

Despite the fact that the model accurately predicts the transition between saturated and unsaturated states, as well as the transition between elastic and elastoplastic states, there are some limitations to the prediction of volumetric deformations. Different alternatives may be considered to increase the precision of the model as, for example, modify the geometry of the yield surface, introduce a non-associated flow rule, or use the bounding surface approach.

Acknowledgements

We are grateful to the support provided by Professor Nasser Khalili and Dr. Arman Khoshghalb at the University of New South Wales in Sydney, Australia. Their ideas and disposition to achieve the experimental program of this project are acknowledged.

We also thank the Mexican National Council for Science and Technology (CONACyT) for their financial support.

References

[1] A. Gens, M. Sánchez, D. Sheng, On constitutive modelling of unsaturated soils, Acta Geotech. 1 (2006).
[2] D. Sheng, Constitutive modelling of unsaturated soils: discussion of fundamental principles, General Report presented at the 5th International Conference on Unsaturated Soils (6–8 September 2010, Barcelona, Spain), in: E.E. Alonso, A. Gens (Eds.), Unsaturated Soils, CRC Press, 2010.
[3] K. Terzaghi, Erdbaumechanik auf Bodenphysikalischer Grundlage, Franz Deuticke, Leipzig and Vienna, 1925.
[4] P. Fillunger, Der Auftrieb in Talsperren, Österreichische Wochenschrift für den öffentlichen Baudienst 1913, pp. 532–556.
[5] A.W. Bishop, The principle of effective stress, Tekn. Ukebl. 106 (1959) 859–863.
[6] L. Laloui, M. Nuth, On the use of the generalised effective stress in the constitutive modelling of unsaturated soils, Comput. Geotech. 36 (2009) 20–23.
[7] E. Juárez-Badillo, Constitutive relationships for soils, in: Symp. on Recent Developments in the Analysis of Soil Behavior and Their Application to Geotechnical Structures, University of New South Wales, NSW, Australia, 1975, pp. 231–257.
[8] E. Rojas, O. Chávez, Volumetric behavior of unsaturated soils, Can. Geotech. J. 50 (2013) 209–222.
[9] E.E. Alonso, A. Gens, A. Josa, A constitutive model for partially saturated soils, Géotechnique 40 (1990) 405–430.
[10] E. Rojas, M.L. Pérez-Rea, T. López-Lara, J.B. Hernández, J. Horta, Use of effective stresses to model the collapse upon, J. Geotech. Geoenviron. Eng. 141 (5) (2015).
[11] E. Calo, K. Sako, K. Araki, Y. Miyamoto, R. Kitamura, A probabilistic and mechanical approach for hysteresis of SWCC in unsaturated soil, in: GeoFrontiers 2011, 2011.
[12] R. Jaafar, W.J. Likos, Estimating water retention characteristics of sands from grain size distribution using idealized packing conditions, ASTM Geotech. Test. J. 34 (2011).
[13] E. Rojas, M.L. Pérez-Rea, G. Gallegos, J. Leal, A porous model for the interpretation of mercury porosimetry tests, J. Porous Media 15 (2012) 517–530.
[14] A. Rostami, G. Habibagahi, M. Ajdari, E. Nikooee, A pore network investigation on hysteresis phenomena and influence of stress state on the SWRC, Int. J. Geomech. 15 (5) (2013).
[15] P.H. Simms, E.K. Yanful, A pore-network model for hydro-mechanical coupling in unsaturated compacted clayey soils, Can. Geotech. J. 42 (2005) 499–514.
[16] A. Koliji, L. Laloui, O. Cuisinier, L. Vulliet, Suction induced effects on the fabric of a structured soil, Transp. Porous Media 64 (2006) 261–278.
[17] Y. Li, N.C. Wardlaw, Mechanisms of nonwetting phase trapping during imbibition at slow rates, J. Colloid Interface Sci. 109 (1986) 473–486.
[18] G. Mason, N.R. Morrow, Capillary behavior of a perfectly wetting liquid in irregular triangular tubes, J. Colloid Interface Sci. 141 (1991) 262–274.
[19] M. Tuller, D. Or, Retention of water in soil and the soil water characteristic curve, in: D. Hillel (Ed.), Encyclopedia of Soils in the Environment, Elsevier Science, Oxford, UK, 2004.
[20] H. Arroyo, E. Rojas, M.L. Pérez-Rea, J. Horta, J. Arroyo, A porous model to simulate the evolution of the soil–water characteristic curve with volumetric strains, C. R. Mecanique 343 (2015) 264–274.
[21] H. Arroyo, E. Rojas, M.L. Pérez-Rea, J. Horta, J. Arroyo, Simulation of the shear strength for unsaturated soils, C. R. Mecanique 341 (2013) 727–742.
[22] E. Rojas, J. Horta, T. López-Lara, J.B. Hernández, A probabilistic solid porous model to determine the shear strength of unsaturated soils, Probab. Eng. Mech. 26 (2011).
[23] R. Thom, R. Sivakumar, V. Sivakumar, E.J. Murray, P. Mackinnon, Pore size distribution of unsaturated compacted kaolin: the initial states and final states following saturation, Géotechnique 57 (2007) 469–474.
[24] E. Ninjgarav, S.G. Chung, W.Y. Jang, C.K. Ryu, Pore size distribution of Pusan clay measured by mercury intrusion porosimetry, KSCE J. Civ. Eng. 11 (2007) 133–139.
[25] R. Hu, Y.-F. Chen, H.-H. Liu, C.-B. Zhou, A water retention curve and unsaturated hydraulic conductivity model for deformable soils: consideration of the change in pore-size distribution, Géotechnique 63 (2013) 1389–1405.
[26] S. Feia, S. Ghabezloo, J.-F. Bruchon, J. Sulem, J. Canou, J.-C. Dupla, Experimental evaluation of the pore-access size distribution of sands, Geotech. Test. J. 37 (2014) 1–9.
[27] G. Della Vecchia, A.-C. Dieudonné, C. Jommi, R. Charlier, Accounting for evolving pore size distribution in water retention models for compacted clays, Int. J. Numer. Anal. Methods Geomech. 39 (7) (2014) 702–723.
[28] F.A.L. Dullien, Porous Media: Fluid Transport and Pore Structure, Academic Press, San Diego, CA, USA, 1992.
[29] W.B. Haines, Studies in the physical properties of soils: IV. A further contribution to the theory of capillary phenomena in soil, J. Agric. Sci. 17 (1927) 264–290.
[30] E. Rojas, O. Chávez, H. Arroyo, T. López-Lara, Modeling the dependency of soil–water retention curve on volumetric deformation, Int. J. Geomech. 17 (2017).
[31] L. Barden, A. McGown, K. Collins, The collapse mechanism in partly saturated soil, Eng. Geol. 7 (1973) 49–60.
[32] A. El Howayek, P. Huang, R. Bisnett, M.C. Santagata, Identification and Behavior of Collapsible Soils, Joint Transportation Research Program, 2011.
[33] Q. Wang, A.M. Tang, Y.-J. Cui, P. Delage, J.-D. Barnichon, W.-M. Ye, The effects of technological voids on the hydro-mechanical behaviour of compacted bentonite–sand mixture, Soil Found. 53 (2013) 232–245.

[34] E. Rojas, Equivalent stress equation for unsaturated soils. I: equivalent stress, Int. J. Geomech. 8 (2008) 285–290.
[35] N. Khalili, S. Zargarbashi, Influence of hydraulic hysteresis on effective stress in unsaturated soils, Géotechnique 60 (2010) 729–734.
[36] M. Nuth, L. Laloui, Effective stress concept in unsaturated soils: clarification and validation of a unified framework, Int. J. Numer. Anal. Methods Geomech. 32 (2008) 771–801.
[37] D.M. Wood, Soil Behaviour and Critical State Soil Mechanics, Cambridge University Press, 1990.
[38] K.H. Roscoe, J.B. Burland, On the generalized stress–strain behavior of 'wet' clay, in: Engineering Plasticity, Cambridge University Press, Cambridge, UK, 1968, pp. 535–609.
[39] M.M. Futai, M.S.S. Almeida, An experimental investigation of the mechanical behaviour of an unsaturated gneiss residual soil, Géotechnique 55 (2005) 201–213.
[40] P. Hervé, H. Tomasz, L. Lyesse, H. LiangBo, Fundamentals of desiccation cracking of fine-grained soils: experimental characterisation and mechanisms identification, Can. Geotech. J. 46 (2009) 1177–1201.
[41] K.C. Power, S.K. Vanapalli, V.K. Garga, A revised contact filter paper method, Geotech. Test. J. 31 (2008).
[42] H.P. Cresswell, T.W. Green, N.J. McKenzie, The adequacy of pressure plate apparatus for determining soil water retention, Soil Sci. Soc. Am. J. 27 (2008) 41–49.
[43] N. Khalili, M.A. Habte, S. Zargarbashi, A fully coupled flow deformation model for cyclic analysis of unsaturated soils including hydraulic and mechanical hysteresis, Comput. Geotech. 35 (2008) 872–889.
[44] Y.J. Cui, P. Delage, Yielding and plastic behaviour of an unsaturated compacted silt, Géotechnique 46 (1996) 291–311.
[45] M. Taiebat, Y.F. Dafalias, Simple yield surface expressions appropriate for soil plasticity, Int. J. Geomech. 10 (2010) 161–169.
[46] X. Gao, T. Zhang, J. Zhou, S.M. Graham, M. Hayden, C. Roe, On stress-state dependent plasticity modeling: significance of the hydrostatic stress, the third invariant of stress deviator and the non-associated flow rule, Int. J. Plast. 27 (2011) 217–231.
[47] T.B. Stoughton, J.W. Yoon, A pressure-sensitive yield criterion under a non-associated flow rule for sheet metal forming, Int. J. Plast. 20 (2004) 705–731.
[48] F. Ma, K. Kishimoto, On yielding and deformation of porous plastic materials, Mech. Mater. 30 (1998) 55–68.
[49] A. Zhou, D. Sheng, An advanced hydro-mechanical constitutive model for unsaturated soils with different initial densities, Comput. Geotech. 63 (2015) 46–66.
[50] A.R. Rusell, N. Khalili, A unified bounding surface plasticity model for unsaturated soils, Int. J. Numer. Anal. Methods Geomech. 30 (2006) 181–212.